

ON THE CORRELATION BETWEEN MULTISCALE MECHANISMS OF DEFORMATION IN UNIAXIAL DYNAMIC STRAINING AND HIGH VELOCITY PENETRATION

Yu.I. Meshcheryakov¹, G.V. Konovalov¹, N.I. Zhgacheva¹, A.K. Divakov¹, E.P. Osokin²

¹Institute of Problems of Mechanical Engineerin RAS, V.O. Bolshoi 61, St. Petersburg, 199178, Russia

²Central Research Institute of Constructional Materials "Prometei", Shpalernaya 14, St. Petersburg, 165114,
Russia

*e-mail: ym38@mail.ru

Abstract. In order to identify the successive stages of developing the hierarchy of multiscale mechanisms of dynamic straining, the shock-induced mesostructure formation is studied in combined experiments. Shock tests of two kinds of aluminum alloy, 1561 and 1565 alloys were conducted in parallel in two regimes of loading: (i) under uniaxial strain conditions and (ii) in high velocity penetration. Combination of loading regimes allows the correlation in formation of multiscale structure depending on strain rate and scheme of shock loading to be traced for both alloys. Formation of mesoscale-1 (1-10 μm) is initiated by the particle velocity pulsations resulted from space polarization of dislocation structure. In 1561 aluminum alloy the structural elements of mesoscale-2 (50-150 μm) are the result of grouping the microshears, whereas in 1565 alloy the mesostructure is the fault formations localized near the boundary of penetration cavern. The strength behavior of both kinds of aluminum alloy proves to be opposite - when resistance to penetration increases, the spall strength decreases.

Keywords: shock loading, multiscale dynamic deformation, high velocity penetration, structural instability, spallation

1. Introduction.

Incorporating the multiscale mechanisms of deformation into description of shock wave processes is thought to be increasingly important. When occur, the multiscale mechanisms include a formation of intermediate scales between macroscale and microscale followed by transient non-equilibrium processes with an attendant transitions from one scale to another. Detailed study of mesoscopic and microscopic levels are now required for the formulation of better models for the macroscopic description of shock phenomena. At least three scales of dynamic deformation have been recognized for over several decades: dislocation scale, mesoscale and macroscale. As for dynamic deformation, two mesoscale sublevels are found: mesoscale-1 (1-10 μm) and mesoscale-2 (50-500 μm) [1]. The transient processes of multiscale dynamic deformation flow in the form of particle velocity fluctuations at each scale level. Modeling of elementary carriers of dynamic deformation as grouping the initially continuously distributed dislocations has been conducted in [2]. Such organized mesoparticles are shown to be nucleated in form of short-living particle accumulations whose chaotic motion in shock wave results in particle velocity pulsations. The velocity pulsations at the mesoscale-1 in the form of particle velocity distribution have been theoretically and

experimentally studied in [3-5]. According to approach developed in [5], the shock-wave front can be presented in form of two-scale configuration including both the mesoscale-1 and mesoscale-2 (Fig. 1). Thus, locally, the front propagates in a pulsating manner with an average velocity V_{macro} as determined from equilibrium consideration of the global conservation laws. Herewith, the experimental technique allows both the average free surface velocity at the mesoscale-2, u_{ms2} , and particle velocity dispersion, D_{ms1} , at the mesoscale-1 to be registered in real time. In this case, the average particle velocity concerns the motion of single element of mesoscale-2 whilst the velocity distribution is measured inside that element. It should be noted that idealized one-dimensional configuration of shock front shown in Fig. 1 reflects the effect only longitudinal components of particle velocity distribution. At the same time, the molecular dynamic simulations demonstrate the presence of transverse components of comparable amplitude [6].

In parallel, the shock-wave experiments under uniaxial strain conditions with using the Line Imaging VISAR (LIV) registration reveal the velocity fluctuations at the mesoscale-2 for tantalum [7] and boron ceramics [8]. These experiments reveal a direct coupling of the particle velocity distribution at the mesoscale-2 with the mechanism of spallation.

Further, simulation of shock-wave propagation with taking into account the particle velocity distribution at the mesoscale has been conducted in [9-11]. The significant result of simulation is a discovery of threshold particle velocity at which the material (polycrystalline copper) transits into structure unstable state whilst the mechanism of dynamic deformation changes from uniform to turbulent.

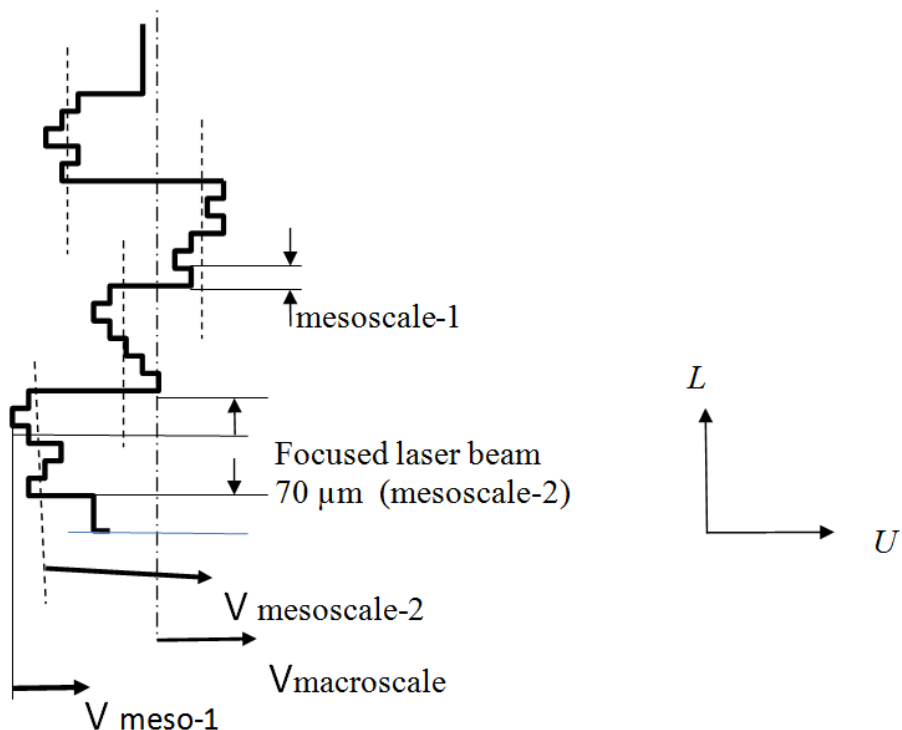


Fig. 1. Space-velocity U-L configurations of multiscale shock front

In the present paper, in order to identify the successive stages of developing the hierarchy of multiscale mechanisms of dynamic straining, the mesostructure formation is studied in combined experiments. A critical step in having an efficient picture of multiscale processes is a parallel application of two schemes of shock loading. The first scheme is the test under uniaxial strain conditions and the second scheme is the high-velocity penetration of

elongated rigid rods. Further, the experiments include the shock tests of two materials, 1561 and 1565 aluminum alloys the quasistatic mechanical characteristics of which are not too different. In high-velocity penetration of rods with plane nose, the impactor faces two mechanisms of resistance to penetration: (i) forehead resistance of plane nose and (ii) friction resistance of side region of rod. In shock tests under uniaxial strain condition, the target suffers only forehead resistance. Comparison of results in both schemes allows the forehead and side resistance of elongated rod to be separated if a need arises.

2. Experimental techniques

To provide a comprehensive analysis of shock tests results, the experiments for each kind of material were conducted in parallel in two schemes of shock loading. The tests under uniaxial strain conditions were conducted with one-stage light gas gun of 37 mm barrel diameter. Plane targets were the discs of 52 mm in diameter and 7 mm thick. Data on dynamic strength and plasticity of material, including dynamic yield limit, spall strength and threshold of structural instability under shock compression were inferred from the temporal profiles of the free surface velocity, $u_{fs}(t)$, which are registered with the interferometer [3,4]. To date the interference is one of the widely used experimental techniques, which allows to measure the mean free surface particle velocity and is the only technique for registering the particle velocity distribution. The quantitative characteristic of particle velocity distribution is the velocity variance (square root of the particle velocity dispersion). The free surface velocity profile in 1561 aluminum alloy target shown in Fig. 2 is a typical for metals deformed under uniaxial strain conditions. This profile provides an information on mean free surface velocity, $u_{fs}(t)$, and velocity variance, $D(t)$, at the mesoscale-1 (0.1-10 μm).

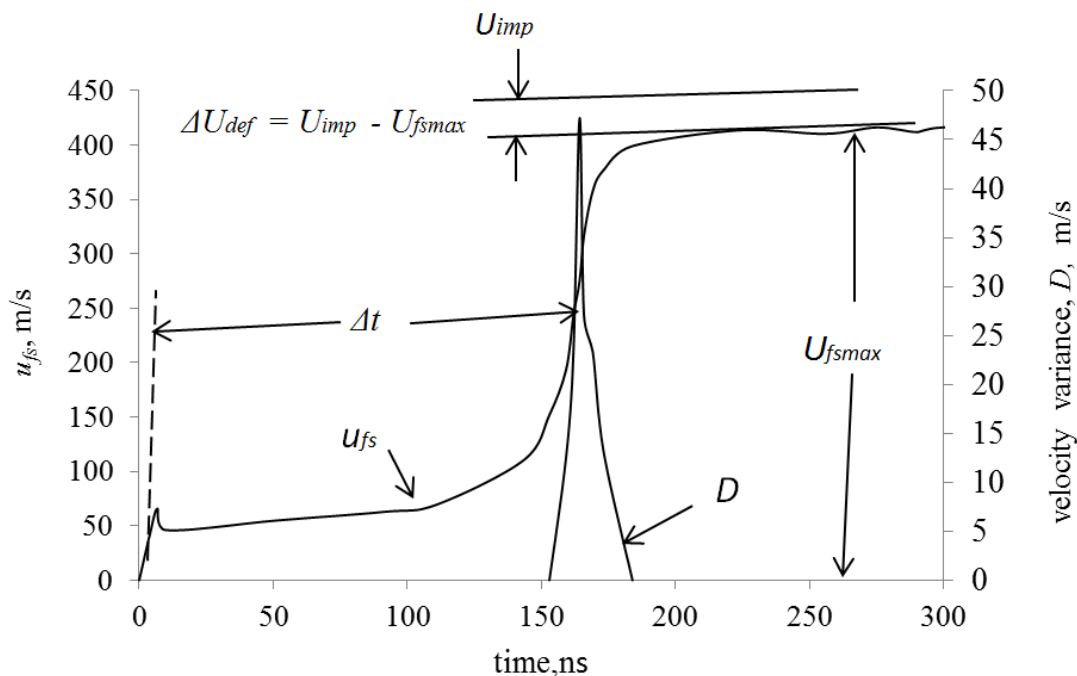


Fig. 2. Free surface velocity profile, $u_{fs}(t)$, and particle velocity variance profile, $D(t)$, for 1561 aluminum alloy target shocked at the impact velocity of 442.5 m/s

One of the basic characteristic of dynamic deformation, which reflects a transition of material into structure-unstable state is a defect of particle velocity which is determined as a difference $\Delta U_{def} = (U_{imp} - U_{fs\max})$ between velocity of impactor under symmetrical collision and maximum free surface velocity at the plateau of compressive pulse (Fig. 2). In our

approach, the maximum free surface velocity $U_{fs\max} = f(U_{imp})$ at which the velocity defect begins to increase drastically is defined as the threshold of structural instability, U_{inst} . Instability threshold characterizes the beginning of shock-induced structural heterogenization of material. This dynamic characteristic can be obtained upon the series of free surface velocity profiles registered under uniaxial strain conditions.

The high velocity penetration tests were performed with the same facility. To provide the perpendicularity relatively plane target, the rod of 20 mm in length and 5 mm in diameter is mounted into poly-vinyl-carbonate sabot (Fig. 3b). The conditions for "rigid rod and target" [12] are provided by using the high-strength 02X18K9M5-VI maraging steel as a material for rod. The typical penetration cavern in 1561 aluminum alloy target is shown in Fig. 4.

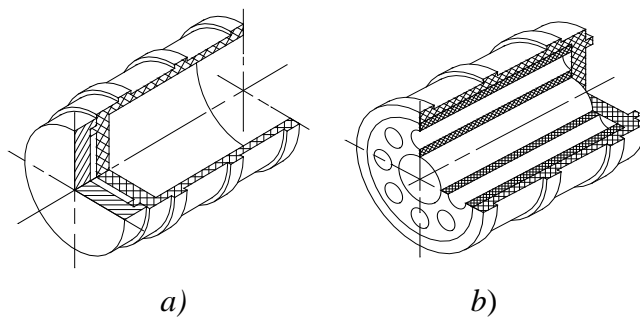


Fig. 3. Impactors for tests under uniaxial strain conditions (a) and penetration tests (b)

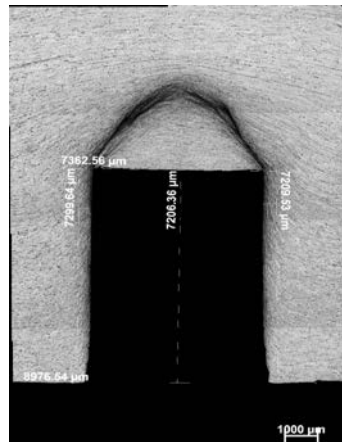


Fig. 4. Penetration cavern in 1561 aluminum alloy at the impact velocity of 450 m/s

The tests on penetration allows an evolution of microstructure to be traced depending on the strain rate. For that, the post shocked targets cut along the wave propagation direction and after polishing and etching were investigated with optical microscope Axio-Observier Z-1m. The quasistatic characteristics of materials are provided in Table 1.

Table 1. Mechanical characteristics of 1565 and 1561 aluminum alloys

Alloy	Target thickness, mm	σ_b , MPa	σ_{02} , MPa	δ , %
Al 1565	7	363	221	15.8
Al 1561	7	353-354	217-224	17.8-18.8

3. Experimental results and analysis

Structural instability threshold and spall strength. To reveal the influence of initial morphology of material on threshold of structural instability, a series of shocks under uniaxial strain conditions within impact velocity range of 250-750 m/s was performed for both alloys. In Fig. 5 the dependencies of maximum free surface velocity, U_{fsmax} , for 1561 and 1565 aluminum alloys are plotted as functions of impact velocity. The dash line corresponds to the equality of impact velocity under symmetrical collision and maximum free surface velocity at the plateau of compressed pulse ($U_{imp} = U_{fsmax}$). The data on maximum free surface velocity as function of impact velocity for each material are approximated with good accuracy by two straight lines directed at different angles to the axis of coordinates. The particle velocity corresponding to change of the slope of dependence $U_{fsmax} = f(U_{imp})$ is accepted to be the threshold of structural instability of material. For 1561 aluminum alloy, the critical change of maximum free surface velocity happens at the impact velocity of 522.9 m/s (instability threshold U_{inst} is indicated with symbol * for 1561 alloy and symbol **) for 1565 alloy). For 1565 aluminum alloy, the critical change of slope for the maximum free surface velocity happens at the impact velocity of 625.3 m/s. The structural instability thresholds are seen to differ by 16 %: $U_{inst} = 506.3$ m/s for 1561 aluminum alloy and $U_{inst} = 588.7$ m/s for 1565 alloy. Thus, the threshold of structural instability proves to be highly sensitive to initial morphology of material.

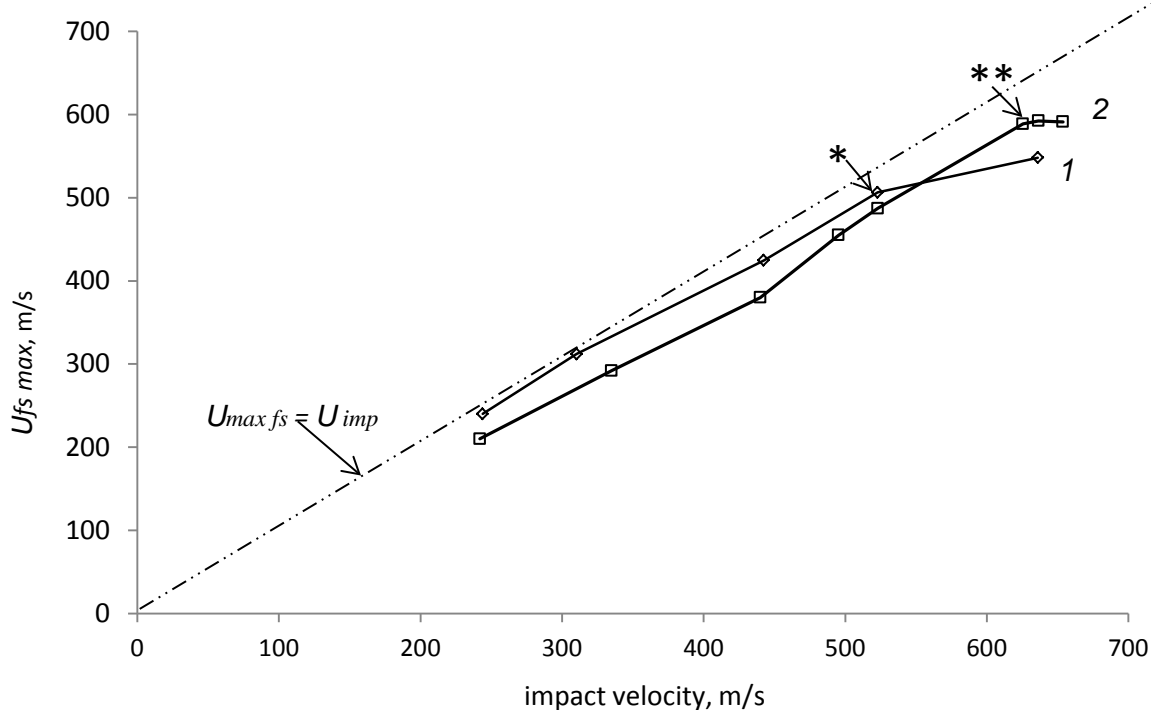


Fig. 5. Dependencies of maximum free surface velocity on impact velocity for 1561 aluminum alloy (1) and 1565 aluminum alloy (2). Thresholds of structural instability are indicated by symbol *) for 1561 alloy and symbol **) for 1565 alloy

It is of interest to first compare the plastic front velocity behavior for both alloys below and beyond of instability threshold. The value of plastic front velocity is determined from the free surface velocity profile as

$$C_{pl} = \frac{h_t}{\frac{h_t}{C_{el}} + \Delta t}, \quad (1)$$

where h_t is the target thickness, C_{pl} is the velocity of plastic front, C_{el} is the longitudinal elastic velocity, Δt is the delay of plastic front relatively elastic precursor. In accordance with [13,14], the value of Δt is measured as a difference in temporal positions of plastic front and elastic precursor midpoints. In Fig. 6 the dependencies of plastic front velocities on impact velocity for both alloys are plotted together. The maximum value of the plastic front velocity for 1561 aluminum alloy is seen to be much smaller as compared to 1565 alloy. For both alloys the plastic front velocity stops to grow just after transition of material into structure-unstable state.

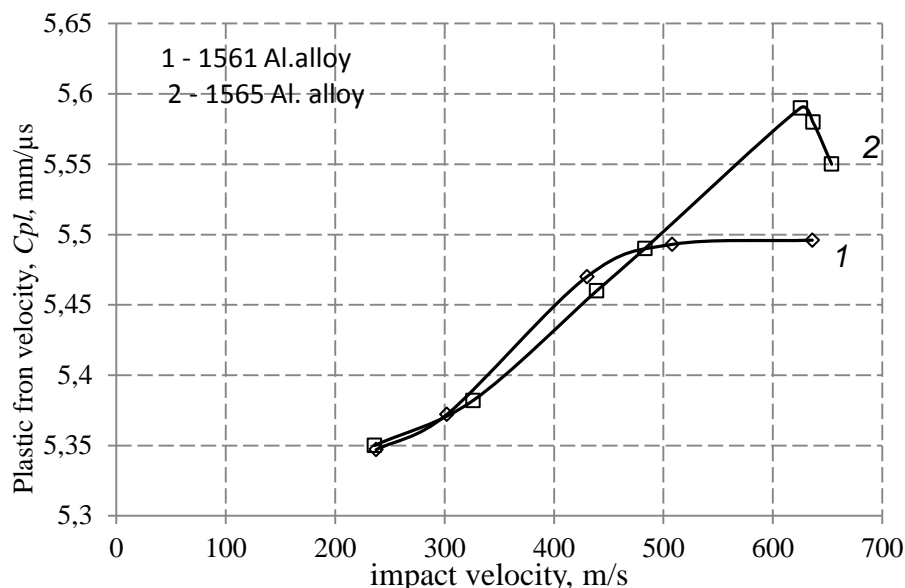


Fig. 6. Dependencies of plastic front velocities on the impact velocity for 1561 (1) and 1565 (2) aluminum alloys

The second dynamic strength characteristic of materials registered in tests under uniaxial strain conditions is the spall strength. Dependencies of spall strength on impact velocity for 1561 and 1565 aluminum alloys are presented in Fig. 7. Comparison of spall dependencies for alloys allows the following conclusions to be done:

- dependencies of spall strength on impact velocity for both materials are non-monotonous;
- the mean value of spall strength for 1561 aluminum alloy is higher than that for 1565 alloy.

Maximum impact velocity which could be registered in shock tests for 1561 alloy doesn't exceed $U_{imp} = 522.9$ m/s. At higher impact velocities, the laser beam of interferometer reflected from the free surface of target is scattered, so the fringe signal disappears.

In Figure 8 the fringe signals for both kinds of alloys are provided. According to working principle of the interferometer, irreversible displacement of fringe signal to upper level means a loss of intensity of laser beam of interferometer reflected from the free surface of target [15].

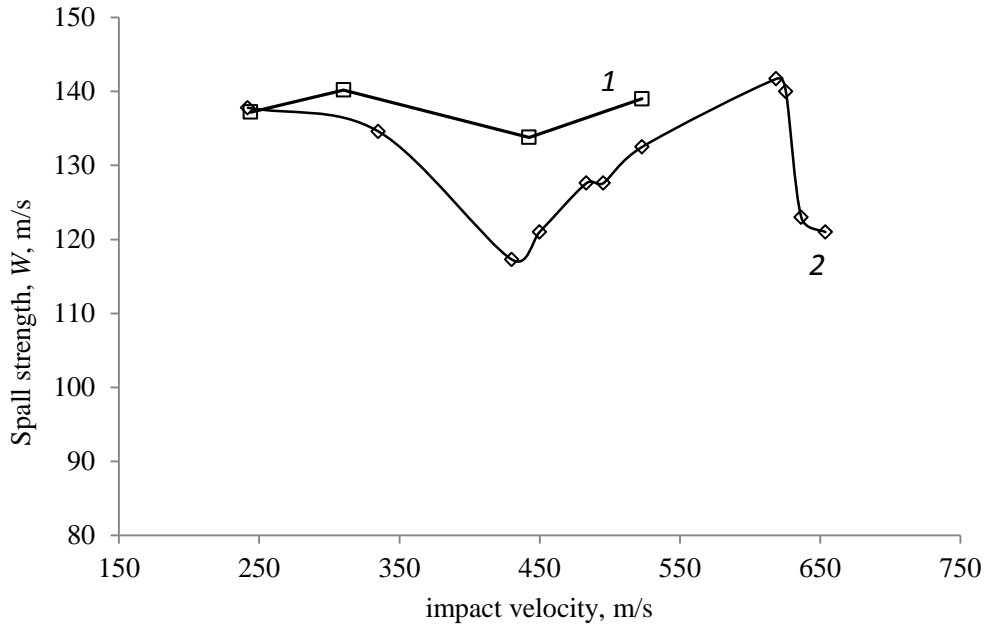


Fig. 7. Dependencies of spall strength on impact velocity for 1561 (1) and 1565 aluminum alloys (2)

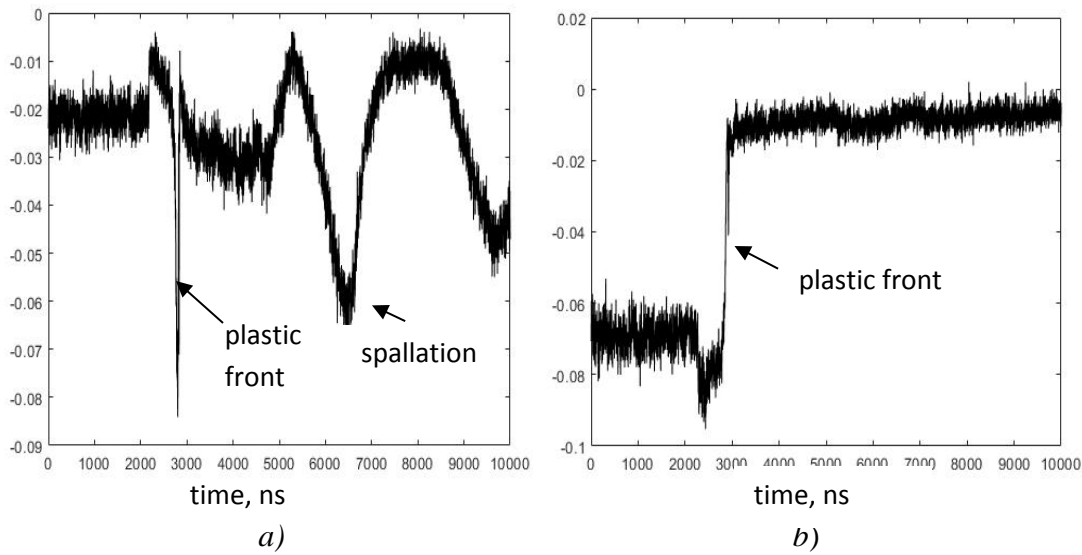


Fig. 8. Fringe signals for 1565 aluminum alloy (a) and 1561 alloy (b) loaded at the impact velocity of ~ 650 m/s

The loss of interference signal occurs only for 1561 alloy. The reason for loss of fringe signal becomes clear after comparison of spall strength $W = f(U_{imp})$ with the maximum free surface velocity $U_{fsmax} = f(U_{imp})$ behavior (Fig. 9), on the one hand side, and data on microstructural investigations of post shocked specimens, on the another hand side (Fig. 10). Dash line in Fig. 9 indicates the maximum impact velocity at which the spall strength could be registered for 1561 alloy. This impact velocity corresponds to break on the curves $U_{fsmax} = f(U_{imp})$ (points D and D') when the material transits into structure unstable state. According to microstructural data, for 1561 alloy this state is characterized by rotation motion of medium (Fig. 9a), which results in loss of the reflective ability of the free surface of target. In this situation, the fringe signal cannot not be registered at the impact velocity higher

522.9 m/s, so the spall strength for that material cannot be measured. As for the 1565 aluminum alloy, dynamic deformation flows in form of translational motion of structural elements of mesoscale-2 (Fig. 10b). The spallation 1565 alloy flows in the form of cleavage. In this case, the chaotic scattering of laser beam at the free surface of target is absent and free surface velocity profile can be registered within overall range of impact velocities. Such behavior of inner structure of 1565 alloy is related to texture of material which prevents to rotational motion of structural elements.

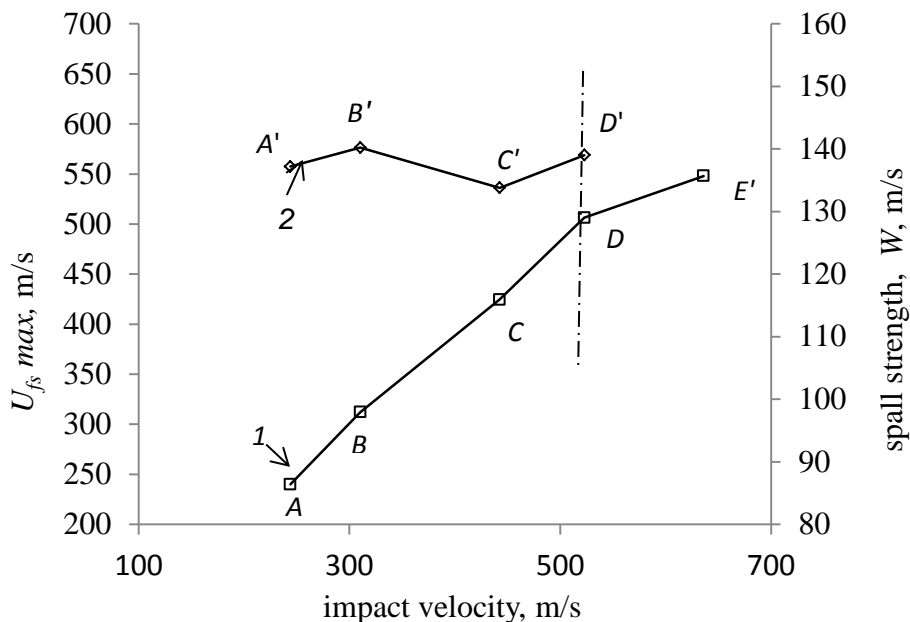


Fig. 9. Maximum free surface velocity (1) and spall strength (2) versus impact velocity for 1561 aluminum alloy

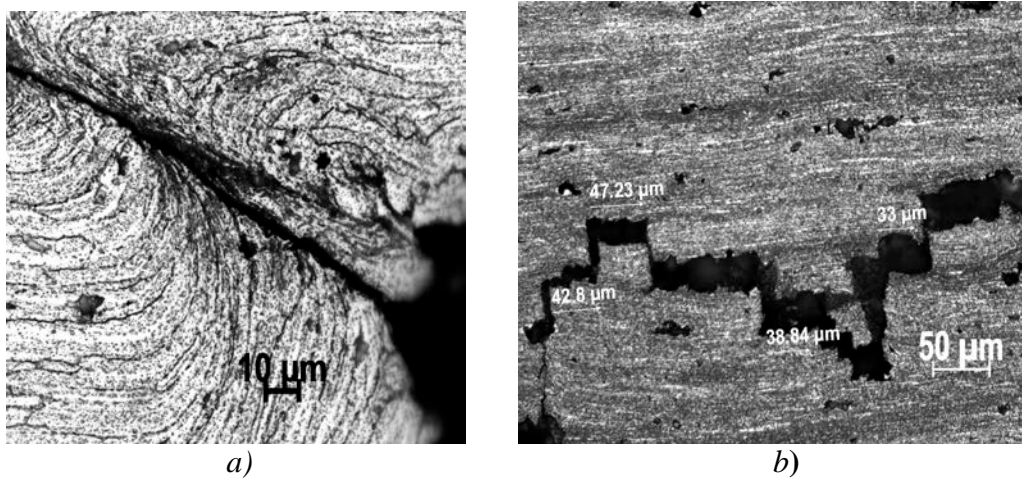


Fig. 10. Morphology of spall zone in 1561 (a) and 1565 (b) aluminum alloy targets

In Figure 11 the dependencies for maximum free surface velocity at the plateau of compressive pulse, U_{fsmax} , and spall strength, W , on the impact velocity for 1565 aluminum alloy are plotted. Both the spall strength and maximum free surface velocity dependencies are non-monotonous, the breaks happen at the identical impact velocities (indicated with dash lines). This means that the internal processes responsible for dynamic deformation and strength for both cases are mutual related. After achieving the instability threshold value of 588.7 m/s at the impact velocity of 625.3 m/s, the spall strength decreases up to minimum for

this material value of ~ 120 m/s. This result testifies that spall strength is determined by the processes at the first front and plateau of compressive pulse and cannot be considered as tensile strength of material.

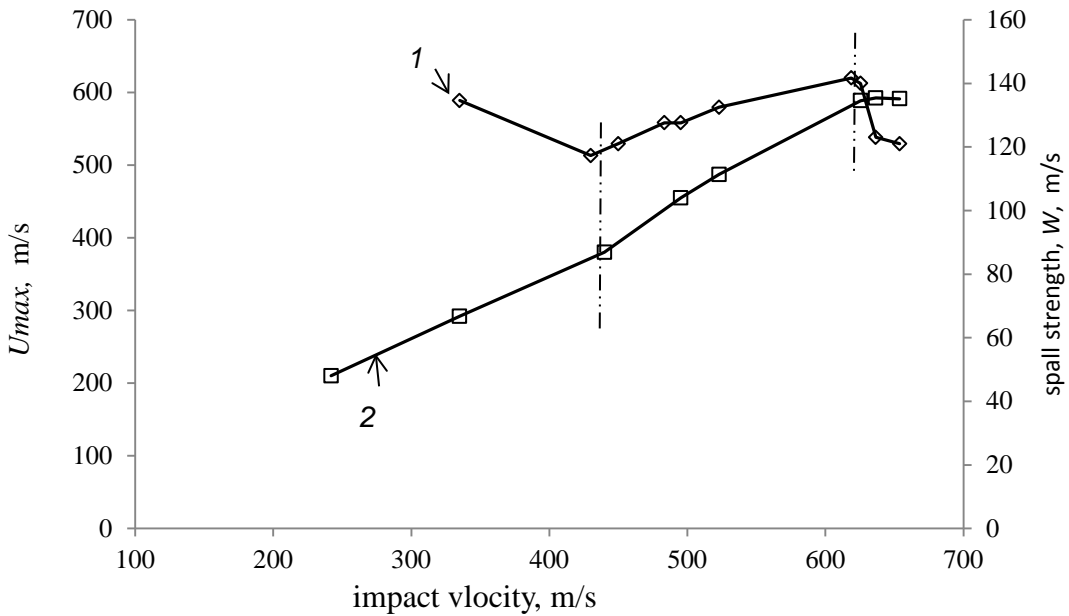


Fig. 11. Dependencies of spall strength, W , (1) and maximum free surface velocity, U_{fsmax} , (2) on the impact velocity for 1565 aluminum alloy

Structural instability threshold and high velocity penetration. Resistance to high velocity penetration is characterized by the value of penetration depth and by the slope of curve $L = f(U_{imp})$ - the smaller the slope of curve, the higher the resistance to penetration. Dependencies of penetration depth on impact velocity, $L = f(U_{imp})$, are provided in Fig. 12. Both materials show practically identical resistance to penetration up to impact velocity of 650-690 m/s after what the resistance to penetration for 1561 aluminum alloy decreases whereas for 1565 alloy the resistance to penetration increases. The breaks at curves are indicated by symbol $^{*)}$ for 1561 aluminum alloy and symbol $^{**})$ for 1565 alloy. Such behavior reflects the fact that usage of 1565 aluminum alloy as defense material is preferable at high region of impact velocities under investigation.

In Figure 13 the penetration depth curve $L = f(U_{imp})$ for 1565 aluminum alloy is plotted together with the dependence of maximum free surface velocity $U_{fsmax} = f(U_{imp})$. The comparison of curves shows that correlation between these processes really exists. The dependence $U_{fsmax} = f(U_{imp})$ determined on the basis of uniaxial strain conditions suffers two breaks - at the impact velocities of 440 m/s and 653.5 m/s. The dependence of penetration depth also suffers two breaks - at the impact velocities of 440 m/s and 677.7 m/s. The critical changes of penetration dependence slope happen just at the strain rate where the breaks of dependence $U_{fsmax} = f(U_{imp})$ occur (dash lines in Fig. 13). Such behavior of curves evidences the common mechanism of interaction of impactor with the inner structure of target in tests under uniaxial strain conditions and rigid rod during the high velocity penetration. It should be noted that two breaks at high region of impact velocities in both schemes of loading also happen at close impact velocities - 653.5 m/s in plane tests and 677.7 m/s in penetration tests. This means that both breaks are of the same nature - forehead resistance to deformation and fracture.

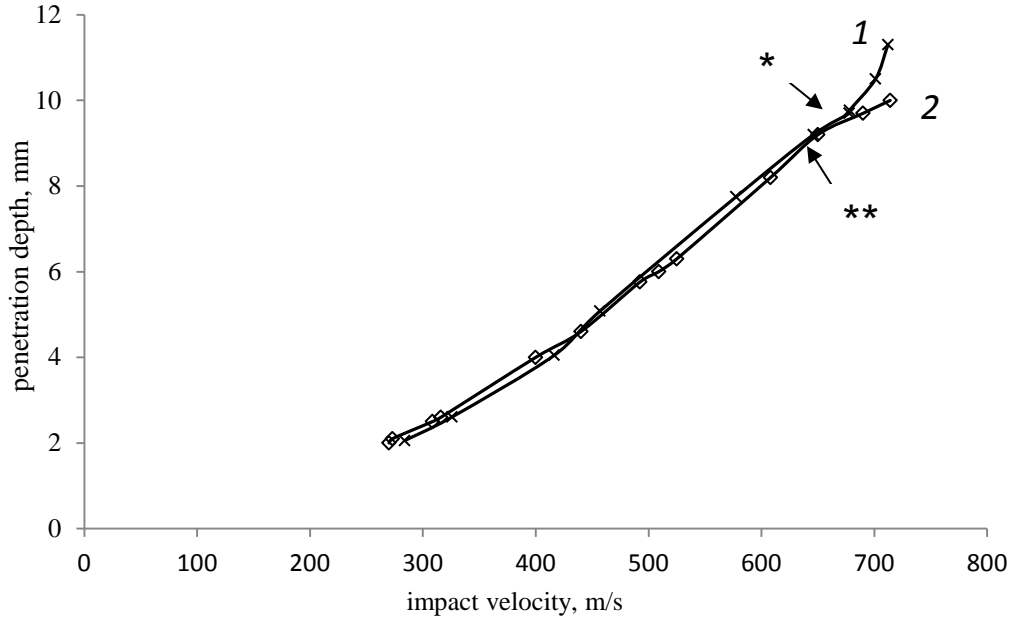


Fig. 12. Dependencies of penetration depth, L , on the impact velocity for 1561 (1) and 1565 (2) aluminum alloys

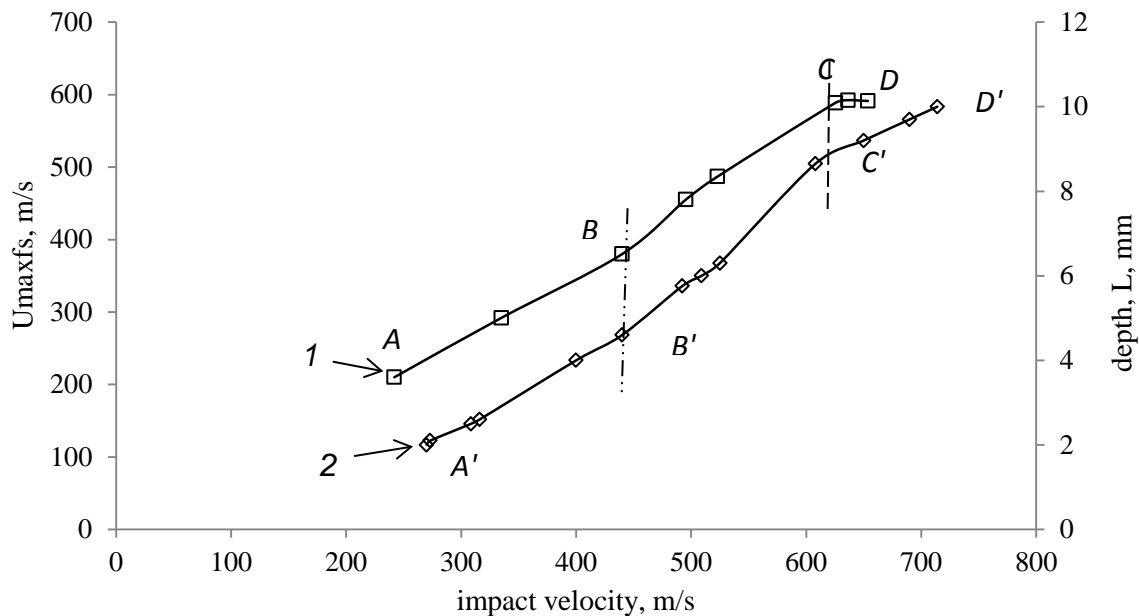


Fig. 13. 1 - dependence of maximum free surface velocity, U_{fmax} ; 2 - dependence of penetration depth, L , on impact velocity for 1565 aluminum alloy

Spall strength and resistance to high velocity penetration. Now let us consider a correlation between spall strength and resistance to penetration. The dependencies of spall strength, W , and penetration depth, L , on the impact velocity for 1565 aluminum alloy are presented in Fig. 14. The correlation of the processes flowing during uniaxial dynamic compression and high-velocity penetration is seen to be evident. Within pieces AB and BC of penetration depth curve, the slope of curve changes at point B : $\frac{dL_{AB}}{dU_{imp}} < \frac{dL_{BC}}{dU_{imp}}$. The resistance to penetration within piece AB of curve (2) is seen to be higher as compared to that for piece BC . At the same time, the spall strength curve shows the opposite trend. Within the piece $A'B'$

the spall strength decreases from 137.8 m/s to 117.3 m/s. After point B' , within piece $B'C'$ $\frac{dW_{B'C'}}{du} > \frac{dW_{A'B'}}{du}$, which means that spall strength increases with the impact velocity increasing. Both critical changes of the material response happen within impact velocity range of 400-440 m/s. Analogous situation is seen after the second critical impact velocity of ~ 630 m/s - within piece CD of penetration curve (2) the slope of curve decreases: $\frac{dL_{CD}}{du} < \frac{dL_{BC}}{du}$, i.e. the resistance to penetration within CD increases. Within the same range of impact velocities, about 600-653 m/s, the spall strength decreases (see curve (1)) Thus, within impact velocity range of 240 - 653 m/s the strength behavior of 1565 aluminum alloy in two schemes of shock loading proves to be opposite - *when resistance to penetration increases, the spall strength decreases.*

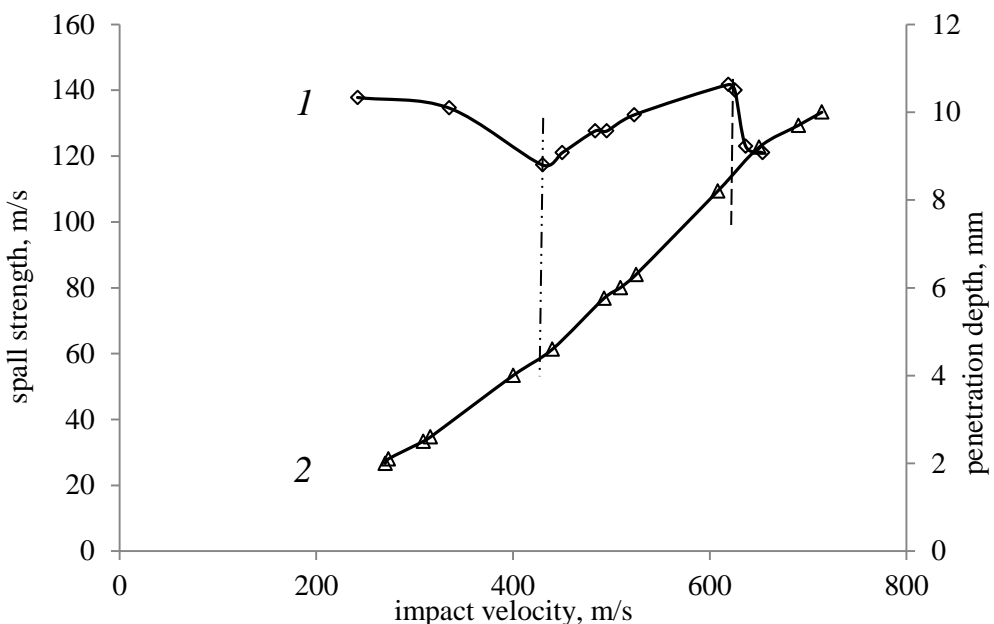


Fig. 14. Dependencies of spall strength (1) and penetration depth (2) on the impact velocity for 1565 aluminum alloy

The analogous correlation between spall strength and resistance to penetration is seen for 1561 alloy. Dependencies $L = f(U_{imp})$ for 1561 alloy are presented in Fig. 15.

For the pieces AB and BC of penetration curve $\frac{dL_{AB}}{du} < \frac{dL_{BC}}{du}$, which means that resistance to penetration within piece AB greater than that for piece BC . Within piece $A'B'$ the spall strength $W = f(U_{imp})$ decreases whilst within piece $B'C'$ the spall strength increases.

Finally, within pieces BC and CD $\frac{dL_{BC}}{du} < \frac{dL_{CD}}{du}$. On the basis of above analysis it may be concluded that mutual behavior of spall strength and resistance to penetration for 1561 aluminum alloy turns out to be analogous that for 1565 aluminum alloy - *when the resistance to penetration increase, the spall strength decreases.*

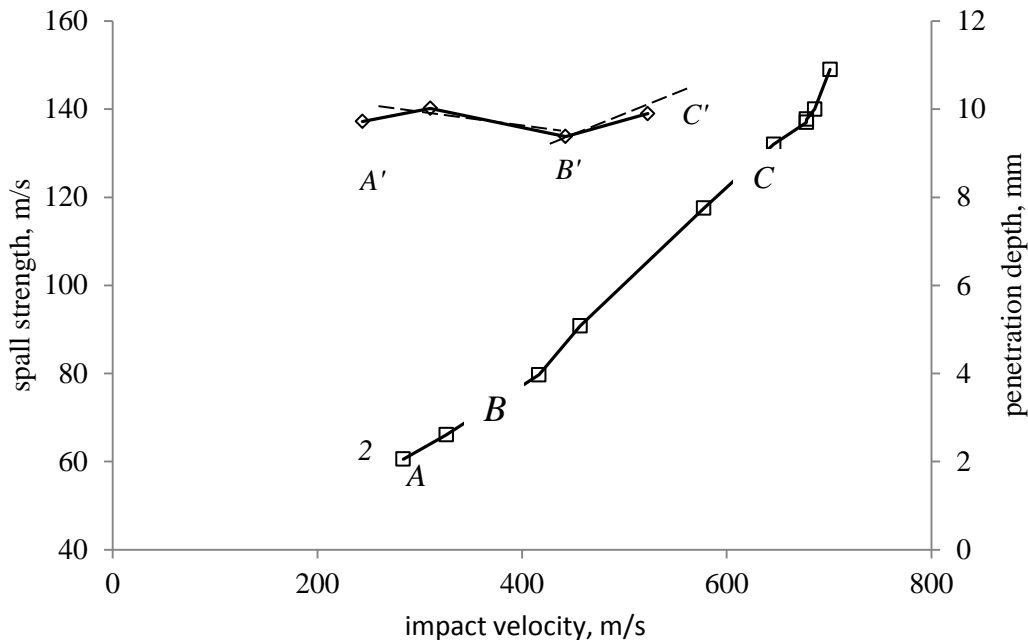


Fig. 15. Dependencies of spall strength (1) and penetration depth (2) on the impact velocity for 1561 aluminum alloy

4. Microstructural investigations

1561 Aluminum alloy. In Figure 16 the micrographs of initial state of grain structure for both alloys are presented. The inner structure for alloys is seen to differ very much - the grain structure of 1561 aluminum alloy consists of equal-axis grains whereas structure of 1565 alloy contains the elongated grains - texture.

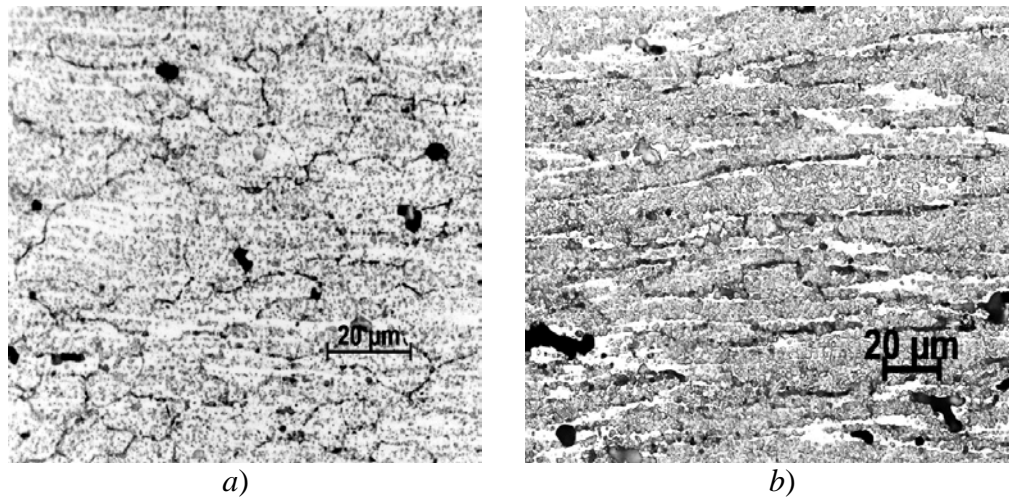


Fig. 16. Initial structural states of 1561 (a) and 1565 (b) aluminum alloys

In Figure 17 the morphology of lateral region of cavern in 1561 aluminum alloy loaded at the impact velocity of 328 m/s is shown. This state of structure corresponds to impact velocity of higher the impact velocity at which the break at the dependence $L=f(U_{imp})$ happens. The numerous microshears oriented along the direction of impact are clearly seen. Nucleation of microshears evidences a transition to new kinematical mechanism of dynamic deformation - instead of uniform deformation, the non-uniform deformation in form of shear banding at the mesoscale-1 is initiated. Formation of above meso-shears is a typical dynamic

effect [16-20]. In the case of dynamic straining, the mesostructure is the totality of short-living formations - mesoparticles. A distinctive feature between mesoparticles is the difference in velocities. A driving force for nucleation of dynamic meso-shears is the mesoparticle velocity pulsations, the quantitative characteristic of them being the particle velocity dispersion D^2 . Nucleation of dynamic mesoparticles is speculated to be the result from the shock-induced space polarization of dislocation structure [19].

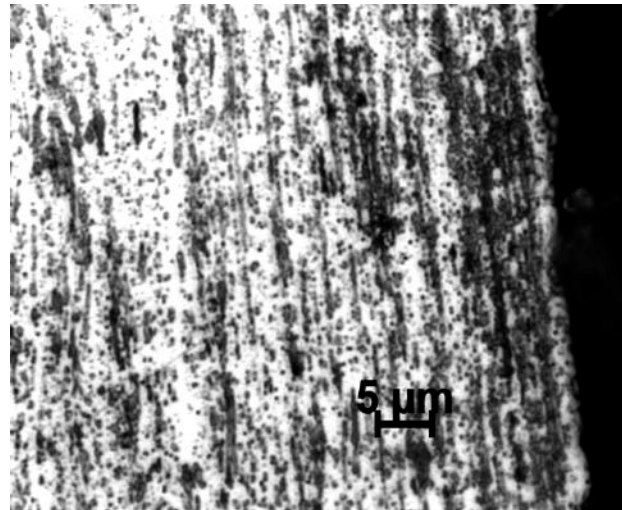


Fig. 17. The morphology of lateral region of cavern in 1561 alloy loaded at the impact velocity of 328 m/s

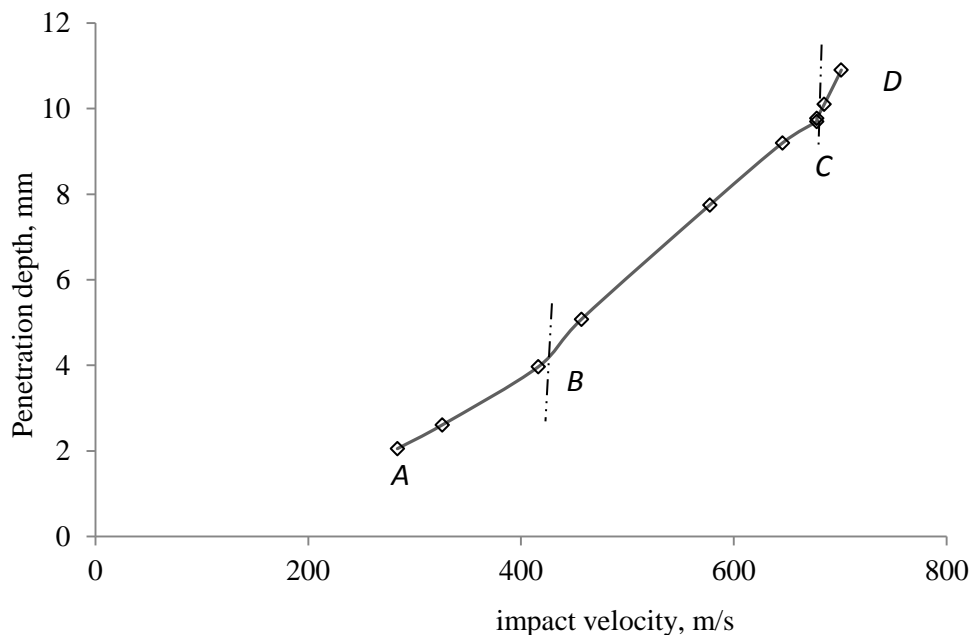


Fig. 18. Dependence of penetration depth on impact velocity for 1561 aluminum alloy

The living time of dynamic mesoparticles in aluminum is found to be of the order of $\Delta t \approx 200$ ns [2], whilst the value of the velocity variance (square root of the particle velocity dispersion) in 1561 aluminum alloy equals $D \approx 45$ m/s (see Fig. 2). Then the mean size of meso-shear equals $L = D \cdot \Delta t = 45(\text{m/s}) \cdot 200(\text{ns}) \approx 9 \mu\text{m}$, which corresponds to structural pattern shown in Fig. 16. In accordance with classification of [1], this size corresponds to mesoscale-1. In Fig. 19-20 three stage of microstructure evolution at the lateral zone of 1561

aluminum alloy target are presented. With the increase of impact velocity, the meso-shears are seen to unite into elongated groups (region *BC* in Fig. 18) and further into elongated cells. The maximum resistance to penetration is realized in region *AB* where uniform dynamic deformation flows. With the beginning of meso-shearing, the resistance to penetration decreases: $\frac{dL_{AB}}{dU_{imp}} < \frac{dL_{BC}}{dU_{imp}}$. This range of impact velocity corresponds to region *BC*. Minimum resistance to penetration for 1561 aluminum alloy corresponds to region *CD*: $\frac{dL_{CD}}{dU_{imp}} < \frac{dL_{BC}}{dU_{imp}}$,

i.e. after ultimate formation of mesoscale-2 in form of elongated cells (Fig. 20).

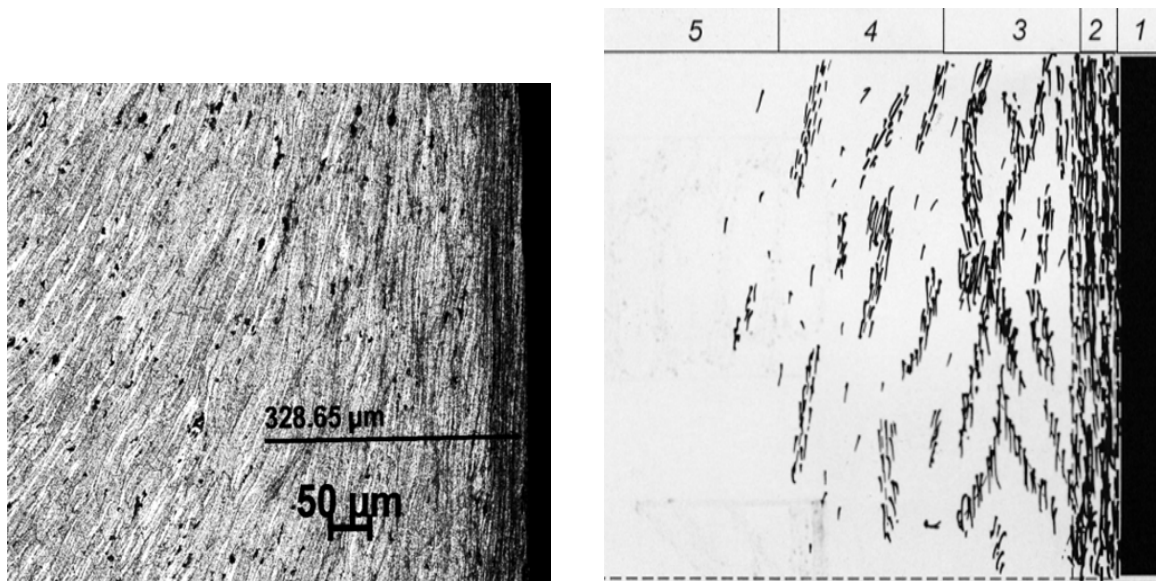


Fig. 19. Initial stage of structure formation at the mesoscale-2 ($U_{imp} = 426$ m/s); 1 – cavern; 2 – zone near the cavern bank; 3 – mesoflows consisting of microshears thickening; 4 – embryos of mesoflows; 5 – free zone

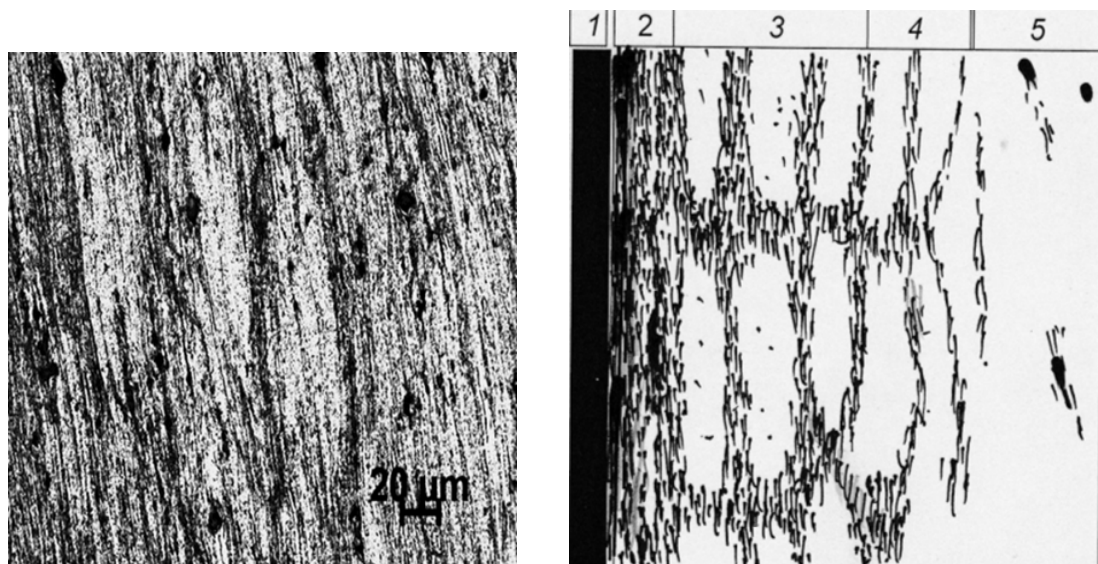


Fig. 20. Final stage of structure formation at the mesoscale-2 in 1561 aluminum alloy ($U_{imp} = 677$ m/s). 1 – region of cavern; 2 – region of microshears thickening near the bank of cavern; 3 – region of mesostructure formation; 4 – region of mesoslow; 5 – free region

1565 aluminum alloy. In Figure 21 together with dependencies for penetration depth $L=f(U_{imp})$, three states of structure for different impact velocities for 1565 aluminum alloy are presented. Because of texture, in this material the cell formations cannot be nucleated. For comparison, in Fig. 22 the states of structure for 1561 and 1565 aluminum alloys are presented. In 1561 alloy at the impact velocity of 645 m/s the microshears join into wide shears and elongated cells of mesoscale-2 (Fig. 22a) whereas in 1565 alloy the microshears remain within boundaries of elongated grains (Fig. 22b).

Nucleation of meso-shears in 1561 alloy results in decreasing the resistance to penetration – after impact velocity of 645 m/s the slope of penetration curve increases (region *CD* in Fig. 18). At the same time, in 1565 alloy the texture prevents to nucleation of meso-shears, which results in increasing the resistance to penetration – after impact velocity of 650 m/s the slope of penetration curve decreases (region *CD* in Fig. 21).

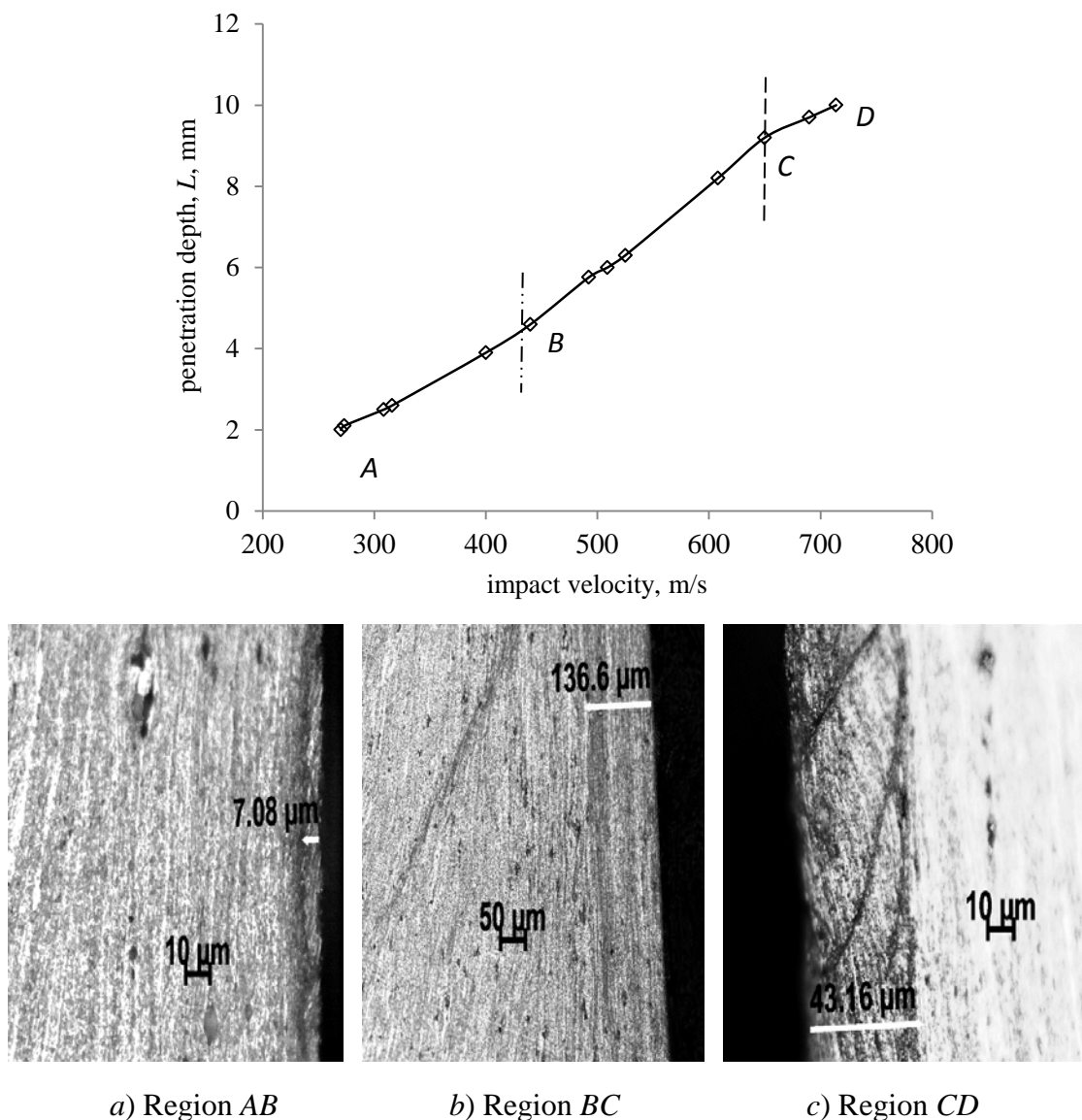


Fig. 21. Three regions of penetration behavior for 1565 alloy depending on impact velocity

The most noteworthy feature of post shocked 1565 aluminum targets is the presence of the highly regular fault structures. Where observed, the fault structures occupy the bank of

cavern in regions *AB* and *CD* of penetration curve in Fig. 17*a*. Simultaneously the resistance to penetration increases, which results in decrease of the slope of penetration curve. At the same time, the regular faults are absent within range of impact velocities of *BC*, where the structure of post shocked material is uniform while the resistance to penetration decreases. It may be concluded that from the point of view of resistance to penetration, the 1565 aluminum alloy turns out to be more preferable at upper region of impact velocities as compared to 1561 alloy. At the same time, as in Fig. 10 shown, the spall strength of 1565 alloy at the upper region of impact velocities decreases.

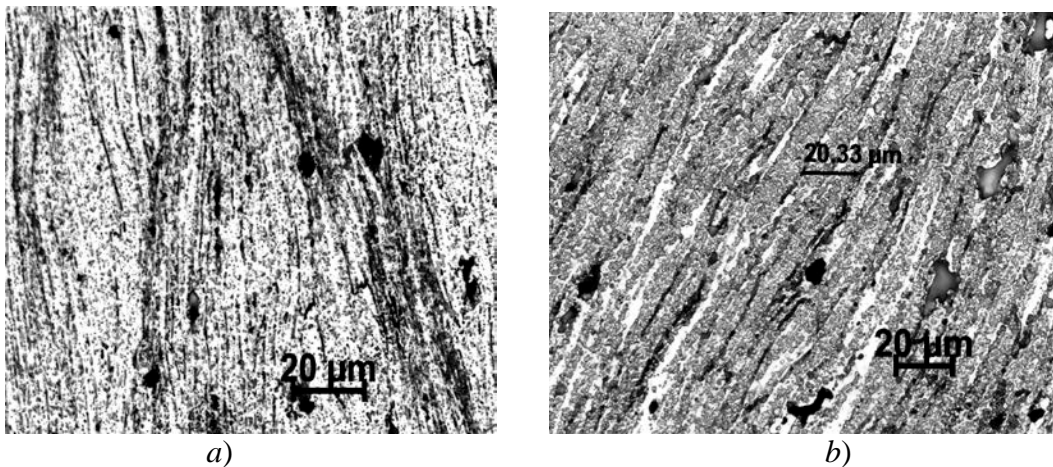


Fig. 22. Uniting the microshear into elongated cells in lateral zone of penetration in 1561aluminum alloy (*a*); microshears localized inside the grain boudaries of texture in 1565 aluminum alloy (*b*)

5. On the resonance excitation of mesoscale

At the impact velocities used, diagnostics with a time resolution of the order of part of nanosecond is sufficient to reveal the internal structure of plastic wave. Specifically, in our experiments, the time resolution of equipment allows to reveal the oscillation structure of plastic front. Previously, the plastic front oscillations have been fixed in copper [21] and theoretically described in [21,22]. Where observed, the oscillations are excited at the top of plastic front. At that position the latter transits into plateau of compressive pulse. This is thought to correspond to transition of dynamic deformation from mesoscale-1 to mesoscale-2. Figure 23 demonstrates the oscillations in 7 mm 1561 aluminum alloy target loaded at the impact velocity of 590 m/s. The oscillations are seen only at the impact velocities higher the threshold of structure unstable transition, U_{inst} . This allows to suppose that excitation of oscillations and non-equilibrium transient processes are mutual coupled phenomena with an attendant transition of material into structure unstable state. The mean period of oscillations of ~ 2 ns corresponds to space period of 10 μm, which coincides with the mean size of micro shear of meso-1 (3-12 μm). Thus, while the mesoscale-1 structures are nucleated owing to particle velocity pulsations, the meso-2 cell-structures are initiated due to resonance interaction of meso-1 structures with the plastic front oscillations.

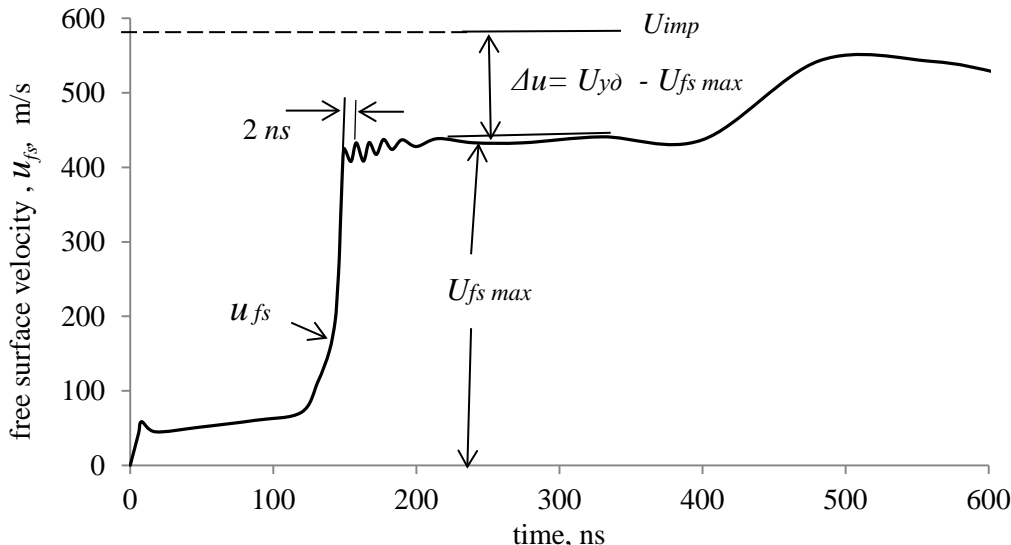


Fig. 23. Free surface velocity profile, u_{fs} , for 7 mm 1561 aluminum alloy target loaded at the impact velocity of 590 m/s

6. Conclusions

1. Shock tests of two kinds of aluminum alloy in two schemes of loading reveal different mechanisms of mesostructure formation depending on initial morphology of material, scheme of shock loading and strain rate. In 1561 aluminum alloy the formation of mesoscale-1 ($3\text{-}12\mu\text{m}$) flows by means of nucleation of mesoshears oriented in the wave propagation direction. With the increase of strain rate the mesoshears are gradually united into cell-structures of mesoscale-2 ($100\text{-}150\mu\text{m}$).
2. Formation of microshears and cell structures decreases the resistance to high velocity penetration. In 1565 aluminum alloy, because of the texture, formation of cell structures is suppressed. In this situation, resistivity to penetration is determined by the fault structures nucleated at the boundary of cavern.
3. At the upper region of impact velocities, 1565 aluminum alloy reveals the increased resistivity to penetration as compared to 1561 alloy.
4. Within impact velocity range of 250 - 750 m/s the strength behavior of alloys proves to be opposite - when resistance to penetration increases, the spall strength decreases.
5. The threshold of structural instability is found to be highly sensitive to initial morphology of material: $U_{inst} = 506.3 \text{ m/s}$ for 1561 aluminum alloy and $U_{inst} = 588.7 \text{ m/s}$ for 1565 alloy.
6. Transition one scale to another happens under resonance conditions for mesostructural elements and plastic front oscillations.

Acknowledgements. No external funding was received for this study.

References

- [1] Panin VE, Egorushkin VE, Panin FV. Physical mesomechanics of deformed solid as multiscale system. 1. Physical basis of multiscale approach. *Physical Mesomechanics*. 2006;9(3): 9-22.
- [2] Meshcheryakov YI, Prokuratova EI. Kinetic theory of continuously distributed dislocations. *International Journal of Solids and Structures*. 1995;3(12): 1711-1726.
- [3] Asay JR, Barker LM. Interferometric measurements of shock-induced internal particle velocity and spatial variation of particle velocity. *J. Appl. Phys.* 1974;45(6): 2540-2546.
- [4] Meshcheryakov YI, Divakov AK. Multiscale kinetics of microstructure and strain-rate dependence of materials. *Dymat Journal*. 1994;1(4): 271-287.

- [5] Meshcheryakov YI, Divakov AK, Zhigacheva NI, Makarevich IP. Dynamic structures in shock-loaded copper. *Physical Review B*. 2008;78(6): 64301-64316.
- [6] Chhabildas LC, Trott WM, Reinhart WD, Cogar IR, Mann GA. Incipient spall structures in tantalum- microstructural effects. In: Furnish MD, Thadani NN, Horie YY. (eds.) *Shock Compression of Condensed Matter-2001*. Atlanta; 2001. p.483-486.
- [7] Meshcheryakov YI. *Multiscale Shock-Wave Processes in Solids*. Saint-Petersburg: Nestor-History; 2018.
- [8] Vogler TJ, Reinhart WD, Chhabildas LC. Dynamic behavior of boron carbide. *J. Appl. Phys.* 2004;95(8): 4173-4183.
- [9] Yano K, Horie Y. Discrete-element modeling of shock compression of polycrystalline copper. *Physical Review B*. 1999;59(21): 13672-13680.
- [10] Case S, Horie Y. Discrete element simulation of shock wave propagation in polycrystalline copper. *Journal of the Mechanics and Physics of Solids*. 2007;55(3): 389-514.
- [11] Baer MR. Computatinal modeling of heterogeneous reactive materials at the mesoscale. In: Furnish MD, Chhabildas LC, Nixon RS. (eds.) *Shock compression of condensed matter-1999*. New York: The APS proceeding; 1999. p.27-33.
- [12] Rozenberg Z, Dekel E. *Terminal ballistics*. New York: Springer; 2012.
- [13] Barker LM. α - phase Hugoniot of iron. *J. Appl. Phys.* 1975;46(6): 2544-2547.
- [14] Swan GW, Duvall GE, Thornhill CK. On steady wave profiles in solids. *Journal of the Mechanics and Physics of Solids*. 1973;21(4): 215-227.
- [15] Zlatin NA, Mochalov SM, Pugachev GS, Bragov AM. Laser differential interferometer. Theory of the device and an example of application. *Soviet Physics Technical Physics*. 1974;18(9): 1235-1237.
- [16] Asay JR, Chhabildas LC. Determination of the shear strength of shock compressed 6061-T6 aluminum. In: Meyers MA, Murr LE. (eds.) *Shock Waves and High-Strain-Rate Phenomena in Metals: Concepts and Applications*. New-York: Plenum Publishing Corporation; 1981.
- [17] Grady DE, Asay JR. Calculation of thermal trapping in shock deformation of aluminum. *J. Appl. Phys.* 1982;83(1): 7350-7354.
- [18] Murr LE, Esquivel EV. Review observation of common microstructural issues associated with dynamic deformation phenomena: twins, microbands, grain size effects, shear bands and dynamic deformation re-crystallization. *Journal of the Material Science*. 2004;39(4): 1153-1168.
- [19] Vladimirov VI, Ivanov VN, Priemskii NM. Mesoscopic level of plastic deformation. In: Zhurkov SI. (ed.) *Physics of Strength and Plasticity*. Moscow: Nauka; 1986. p.69-80.
- [20] Khantuleva TA, Meshcheryakov YI. Mesoscale plastic flow instability in a solid under high-rate deformation. *Physical Mesomechanics*. 2017;20(4): 417-424.
- [21] Indeitzev DA, Meshcheryakov YI, Kuchmin AY, Vavilov DS. Multiscale model of steady-wave shock in a medium with relaxation. *Acta Mechanica*. 2015;226(3): 917-930.
- [22] Meshcheryakov YI. Particle velocity non-uniformity and steady-wave propagation. *Shock Waves*. 2017;27(2): 291-297.